Inorg. Chem. **2007**, *46*, 8511–8523

Spectroscopic and Computational Studies of Ni^{3+} Complexes with Mixed S/N Ligation: Implications for the Active Site of Nickel Superoxide Dismutase

Adam T. Fiedler and Thomas C. Brunold*

Department of Chemistry, University of Wisconsin—Madison, 1101 W. University Avenue, Madison, Wisconsin 53706

Received July 4, 2006

Both Ni-containing superoxide dismutase (NiSOD) and NiFe hydrogenases feature thiolate-rich active sites that are capable of stabilizing the Ni^{3+} oxidation state in catalytically relevant species. In an effort to better understand the role of Ni^{3+}–S bonding interactions in these metalloenzymes, we have employed various spectroscopic and computational methods to probe the geometric and electronic structures of three Ni^{3+} complexes with mixed S/N ligation: $[Ni^{3+}(pdtc)_2]^-$ (**1**), $[Ni^{3+}(emb)]^-$ (**2**), and $[Ni^{3+}(ema)]^-$ (**3**) [where pdtc is pyridine-2,6-bis(monothiocarboxylate) and emb and ema are the tetraanions of *N*,*N*′-ethylenebis(*o*-mercaptobenzamide) and *N*,*N*′-ethylenebis(2-mercaptoacetamide), respectively]. Each complex has been examined with electronic absorption, magnetic circular dichroism, electron paramagnetic resonance, and resonance Raman (rR) spectroscopies. Detailed assignments of the features observed in the corresponding spectra have been established within the framework of density functional theory calculations that provide remarkably accurate reproductions of the absorption spectra, *g* values, and vibrational frequencies. Collectively, our spectroscopic and computational studies have yielded experimentally validated electronic-structure descriptions for **1**–**3** that provide significant insights into the nature of the Ni^{3+}–S bonding interactions. Additionally, the results obtained in these studies reveal that the thermochromism observed for **2** is due to the formation of a dimeric species at reduced temperatures, the structure of which has been determined through computational analysis of viable dimer models. Finally, we have employed the framework established in our spectroscopic and computational studies of the Ni^{3+} models to carry out a detailed analysis of our rR data of NiSOD obtained previously. Our results indicate that the Ni^{3+}–S bonds in oxidized NiSOD are significantly stronger than those in **1**–**3** due to the unique mixed amine/amide ligation that is present at the enzyme active site.

1. Introduction

Found primarily in *Streptomyces* bacteria, Ni-containing superoxide dismutase (NiSOD) detoxifies the superoxide radical by catalyzing its disproportionation to molecular oxygen and hydrogen peroxide.[1−4] Structural studies have revealed that, in the oxidized form of the enzyme ($NiSOD_{ox}$), the low-spin ($S = {}^1/_2$) Ni^{3+} center exists in a square-pyramidal coordination environment in which the imidazole ring of the His1 residue serves as the axial ligand (Chart 1).[5−7] The four equatorial ligands include two thiolates from Cys2 and Cys6 in a cis arrangement, the deprotonated amide of the Cys2 backbone (N_{Cys2}), and the N-terminal amine group of His1 (N_{His1}). The reduced state ($NiSOD_{red}$) features a low-spin ($S = 0$) Ni^{2+} center in a square-planar geometry, as the axial His1 ligand dissociates upon metal ion reduction. The role of this unique NiSOD ligand set in activating the Ni

* To whom correspondence should be addressed. E-mail: brunold@chem.wisc.edu.

(1) Youn, H. D.; Kim, E. J.; Roe, J. H.; Hah, Y. C.; Kang, S. O. *Biochem. J.* **1996**, *318*, 889.
(2) Youn, H. D.; Youn, H.; Lee, J. W.; Yim, Y. I.; Lee, J. K.; Hah, Y. C.; Kang, S. O. *Arch. Biochem. Biophys.* **1996**, *334*, 341.
(3) Lee, J. W.; Roe, J. H.; Kang, S. O. *Superoxide Dismutase* **2002**, *349*, 90.
(4) Palenik, B.; Brahamsha, B.; Larimer, F. W.; Land, M.; Hauser, L.; Chain, P.; Lamerdin, J.; Regala, W.; Allen, E. E.; McCarren, J.; Paulsen, I.; Dufresne, A.; Partensky, F.; Webb, E. A.; Waterbury, J. *Nature* **2003**, *424*, 1037.
(5) Barondeau, D. P.; Kassmann, C. J.; Bruns, C. K.; Tainer, J. A.; Getzoff, E. D. *Biochemistry* **2004**, *43*, 8038.
(6) Wuerges, J.; Lee, J. W.; Yim, Y. I.; Yim, H. S.; Kang, S. O.; Carugo, K. D. *Proc. Natl. Acad. Sci. U.S.A.* **2004**, *101*, 8569.
(7) Choudhury, S. B.; Lee, J. W.; Davidson, G.; Yim, Y. I.; Bose, K.; Sharma, M. L.; Kang, S. O.; Cabelli, D. E.; Maroney, M. J. *Biochemistry* **1999**, *38*, 3744.

10.1021/ic061237k CCC: $37.00
Published on Web 02/17/2007

Chart 1. Structures of the NiSOD Active Site in Oxidized (Left) and Reduced (Right) States[5,6]

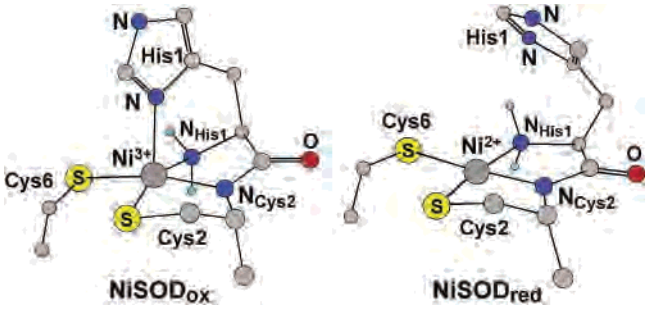

center for catalysis was recently explored in a combined spectroscopic and computational study.[8]

The presence of thiolate ligands in the NiSOD active site was initially surprising because S-containing moieties are susceptible to modification and degradation by oxidants (e.g., superoxide and peroxide) and S ligation was previously unprecedented in the SOD family. However, nickel thiolate coordination is ubiquitous in Ni-containing enzymes that access different oxidation states in their catalytic cycles.[9,10] Other members of this class include acetyl coenzyme A synthase (ACS),[11−13] CO dehydrogenase,[14,15] NiFe hydrogenase,[16,17] and methyl coenzyme M reductase.[18] While these enzymes exhibit considerable diversity in their active-site structures, a common motif is the presence of nickel thiolate coordination, which is crucial in lowering the redox potentials of the corresponding Ni centers. Additionally, Cys ligation is found in the high-affinity Ni-binding site of NikR, a transcription factor that regulates Ni uptake in *Escherichia coli*.[19] Thus, the biological utilization of Ni in various systems is largely dependent upon the ability of thiolate donors to adjust the catalytic, redox, and/or binding properties of Ni centers.

Of the redox-active Ni enzymes mentioned above, only NiSOD[7,8] and NiFe hydrogenases[20] are capable of stabilizing the Ni^{3+} oxidation state in their active sites, although some catalytic cycles proposed for ACS have invoked transient intermediates with Ni^{3+} centers.[21,22] The scarcity of this

Chart 2. Synthetic Models of the NiSOD Active Site

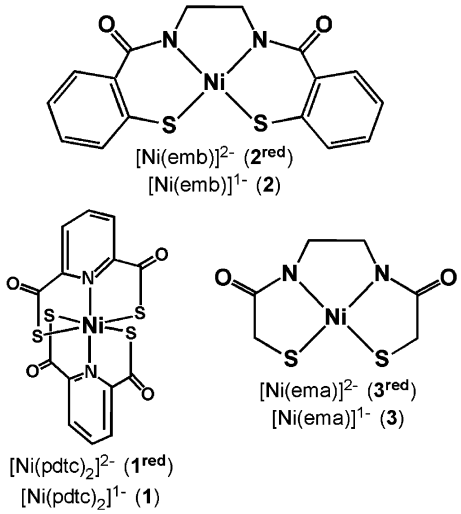

oxidation state in biological systems suggests that Ni^{3+} species with S coordination are intrinsically unstable, a conclusion supported by the relatively small number of synthetic Ni^{3+}−S complexes that have been reported in the literature.[23] While there is an abundance of potential Ni^{2+}−S precursors, such complexes tend to undergo oxidation at the S ligand and not the Ni center. For example, several groups have demonstrated that nickel(2+) thiolate complexes with amine N-donor ligands react with O_2 at S to yield coordinated sulfinate ligands.[24−29] Moreover, one-electron oxidation of these complexes is irreversible and typically leads to sample decomposition via disulfide production.[30−32]

Despite these difficulties, Holm and Kruger were able to synthesize an extensive series of six- and four-coordinate Ni^{3+} complexes with mixed S/N ligation,[33−36] three of which are shown in Chart 2. Instrumental to their success was the utilization of tetraanionic ligand frameworks, which sufficiently depress the $Ni^{3+/2+}$ redox potentials relative to those of the S-containing ligands to allow for metal-centered oxidation. For instance, the pyridine-2,6-bis(monothiocarboxylate) (pdtc) ligands found in complex $[Ni^{3+}(pdtc)_2]^-$ (**1**)

(8) Fiedler, A. T.; Bryngelson, P. A.; Maroney, M. J.; Brunold, T. C. *J. Am. Chem. Soc.* **2005**, *127*, 5449.
(9) Maroney, M. J. *Curr. Opin. Chem. Biol.* **1999**, *3*, 188.
(10) Watt, R. K.; Ludden, P. W. *Cell. Mol. Life Sci.* **1999**, *56*, 604.
(11) Svetlitchnyi, V.; Dobbek, H.; Meyer-Klaucke, W.; Meins, T.; Thiele, B.; Romer, P.; Huber, R.; Meyer, O. *Proc. Natl. Acad. Sci. U.S.A.* **2004**, *101*, 446.
(12) Darnault, C.; Volbeda, A.; Kim, E. J.; Legrand, P.; Vernede, X.; Lindahl, P. A.; Fontecilla-Camps, J. C. *Nature Struct. Biol*. **2003**, *10*, 271.
(13) Doukov, T. I.; Iverson, T. M.; Seravalli, J.; Ragsdale, S. W.; Drennan, C. L. *Science* **2002**, *298*, 567.
(14) Drennan, C. L.; Heo, J. Y.; Sintchak, M. D.; Schreiter, E.; Ludden, P. W. *Proc. Natl. Acad. Sci. U.S.A.* **2001**, *98*, 11973.
(15) Dobbek, H.; Svetlitchnyi, V.; Gremer, L.; Huber, R.; Meyer, O. *Science* **2001**, *293*, 1281.
(16) Higuchi, Y.; Yagi, T.; Yasuoka, N. *Structure* **1997**, *5*, 1671.
(17) Volbeda, A.; Charon, M. H.; Piras, C.; Hatchikian, E. C.; Frey, M.; Fontecilla-Camps, J. C. *Nature* **1995**, *373*, 580.
(18) Ermler, U.; Grabarse, W.; Shima, S.; Goubeaud, M.; Thauer, R. K. *Science* **1997**, *278*, 1457.
(19) Schreiter, E. R.; Sintchak, M. D.; Guo, Y. Y.; Chivers, P. T.; Sauer, R. T.; Drennan, C. L. *Nat. Struct. Biol.* **2003**, *10*, 794.
(20) Davidson, G.; Choudhury, S. B.; Gu, Z. J.; Bose, K.; Roseboom, W.; Albracht, S. P. J.; Maroney, M. J. *Biochemistry* **2000**, *39*, 7468.
(21) Seravalli, J.; Kumar, M.; Ragsdale, S. W. *Biochemistry* **2002**, *41*, 1807.
(22) Ragsdale, S. W. *Crit. Rev. Biochem. Mol. Biol.* **2004**, *39*, 165.
(23) Halcrow, M. A.; Christou, G. *Chem. Rev.* **1994**, *94*, 2421.
(24) Grapperhaus, C. A.; Mullins, C. S.; Kozlowski, P. M.; Mashuta, M. S. *Inorg. Chem.* **2004**, *43*, 2859.
(25) Kaasjager, V. E.; Bouwman, E.; Gorter, S.; Reedijk, J.; Grapperhaus, C. A.; Reibenspies, J. H.; Smee, J. J.; Darensbourg, M. Y.; Derecskei-Kovacs, A.; Thomson, L. M. *Inorg. Chem.* **2002**, *41*, 1837.
(26) Grapperhaus, C. A.; Darensbourg, M. Y. *Acc. Chem. Res.* **1998**, *31*, 451.
(27) Grapperhaus, C. A.; Maguire, M. J.; Tuntulani, T.; Darensbourg, M. Y. *Inorg. Chem.* **1997**, *36*, 1860.
(28) Mirza, S. A.; Day, R. O.; Maroney, M. J. *Inorg. Chem.* **1996**, *35*, 1992.
(29) Mirza, S. A.; Pressler, M. A.; Kumar, M.; Day, R. O.; Maroney, M. J. *Inorg. Chem.* **1993**, *32*, 977.
(30) Colpas, G. J.; Kumar, M.; Day, R. O.; Maroney, M. J. *Inorg. Chem.* **1990**, *29*, 4779.
(31) Kruger, H. J.; Holm, R. H. *Inorg. Chem.* **1989**, *28*, 1148.
(32) Nakabayashi, Y.; Masuda, Y.; Sekido, E. *J. Electroanal. Chem.* **1986**, *205*, 209.
(33) Kruger, H. J.; Peng, G.; Holm, R. H. *Inorg. Chem.* **1991**, *30*, 734.
(34) Kruger, H. J.; Holm, R. H. *J. Am. Chem. Soc.* **1990**, *112*, 2955.
(35) Kruger, H. J.; Holm, R. H. *Inorg. Chem.* **1987**, *26*, 3645.
(36) Hanss, J.; Kruger, H. J. *Angew. Chem., Int. Ed.* **1998**, *37*, 360.

provide four equatorial thiocarboxylate ligands and two axial pyridine donors, resulting in a low $Ni^{3+/2+}$ potential of +150 mV (vs normal hydrogen electrode, NHE).[34] Similarly, the Ni^{3+} state is greatly stabilized by the use of anionic amide groups—as opposed to neutral amine N donors—in the four-coordinate $[NiS_2N_2]$ complexes **2** and **3**, which are reversibly oxidized at potentials of $E_{1/2} = +200$[35] and −100 mV,[33] respectively. Interestingly, it appears that nature employs the same strategy for stabilizing Ni^{3+} centers in biological systems. Our previous studies have demonstrated that the deprotonated amide ligand found at the NiSOD active site (N_{Cys2} in Chart 1) is necessary to ensure Ni-based over S-based oxidation.[8] Furthermore, the low reduction potential of the Ni^{3+} center in the heterobimetallic cluster of NiFe hydrogenase (−160 mV for *D. gigas* hydrogenase) is due to its coordination by four Cys thiolates.[37]

The Ni^{3+} complexes initially synthesized by Holm and Kruger[33−36] provide ideal systems through which to develop a better understanding of the Ni^{3+}−S bonding interactions that are vitally important for redox-active Ni enzymes like NiSOD, NiFe hydrogenase, and (potentially) ACS. Thus, we engaged in detailed studies of the Ni^{3+} complexes **1**, $[Ni^{3+}(emb)]^-$ (**2**), and $[Ni^{3+}(ema)]^-$ (**3**) [where emb and ema are the tetraanions of *N*,*N*′-ethylenebis(*o*-mercaptobenzamide) and *N*,*N*′-ethylenebis(2-mercaptoacetamide), respectively] (Chart 2) using electronic absorption, magnetic circular dichroism (MCD), resonance Raman (rR), and electron paramagnetic resonance (EPR) spectroscopies. Analysis of the experimental data was facilitated by computing spectroscopic parameters using density functional theory (DFT) calculations, which also provided bonding descriptions. This combined spectroscopic/computational approach yielded definitive assignments for the absorption and vibrational features of these Ni^{3+} complexes and afforded comprehensive descriptions of their electronic structures. The implications of these results with respect to the possible roles played by the Ni^{3+}−S bonding interactions in NiSOD and other redox-active Ni enzymes are discussed.

2. Experimental and Computational Methods

Complex Syntheses. All reagents were purchased from Aldrich and used as obtained. Complexes **1**, $\mathbf{2^{red}}$, and $\mathbf{3^{red}}$ were synthesized according to published procedures[33−35,38] and characterized with electronic absorption and ^1H NMR spectroscopies. The oxidized complexes **2** and **3** were generated by treating their Ni^{2+} precursors in acetonitrile (MeCN), dimethyl sulfoxide (DMSO), or *N*,*N*-dimethylformamide (DMF) solutions with a small amount of concentrated I_2 dissolved in the same solvent, as described previously by Yamamura et al.[39] Formation of the Ni^{3+} species was confirmed by characterizing the resulting solutions with electronic absorption and EPR spectroscopies.

Spectroscopy. Room temperature (RT) absorption spectra were collected with a Varian Cary 5E UV−vis−NIR spectrophotometer. Low-temperature electronic absorption and MCD spectra were obtained using a Jasco J-715 spectropolarimeter in conjunction with an Oxford Instruments SM-4000 8T magnetocryostat. For low-temperature absorption and MCD studies, solid-state samples of **1** were prepared as uniform mulls in poly(dimethylsiloxane), while solution samples of **2** and **3** were generated in a 1:1 solvent mixture of propionitrile and butyronitrile to ensure glass formation upon freezing. All MCD spectra reported herein were obtained by subtracting the −7 T spectrum from the +7 T spectrum to eliminate potential artifacts arising from glass strain. X-band EPR spectra were obtained using a Bruker ESP 300E spectrometer equipped with an Oxford ESR 900 continuous-flow liquid-He cryostat.

rR spectra were obtained upon excitation with a Coherent I-302C Kr^+ laser with ∼10−35 mW of laser power at the sample. The scattered light was collected using a ∼135° backscattering arrangement, dispersed by an Acton Research triple monochromator equipped with 1200 groves mm^{-1} gratings, and analyzed with a Princeton Instruments Spec X:100BR deep depletion, back-thinned CCD camera. Solid-state samples of **1** were prepared by thoroughly grinding the sample with a slight excess of KBr in an agate mortar (a small amount of K_2SO_4 was added as an internal reference) in a glovebox. Solution samples of **2** and **3** were prepared in MeCN with concentrations ranging from 0.5 to 5.0 mM. Spectra were accumulated at 77 K by inserting the samples (contained in an NMR tube) in an EPR dewar filled with liquid N_2 to prevent sample degradation during data collection. rR excitation profiles were measured by quantifying the sample peak intensities relative to that of the either the 450 cm^{-1} peak of K_2SO_4 or the 390 cm^{-1} solvent peak of frozen MeCN. All points included in the rR excitation profiles represent the average of at least two data sets. Polarized rR spectra were obtained by filtering both the incident and scattered laser light through polarizers aligned in either a parallel or perpendicular fashion. Normal coordinate analyses (NCAs) were performed using a general valence force field, as implemented in the QCPE program 576 developed by Peterson and McIntosh.

Computational Methods. Geometry optimizations of complexes **1**−**3** were performed with the Amsterdam Density Functional (ADF) 2004.01 software package.[40−43] These optimizations were carried out on a cluster of 20 Intel Xeon processors (Ace computers) using ADF basis set IV (triple-ζ with single polarization on the ligand atoms), an integration constant of 4.0, and the Vosko−Wilk−Nusair local density approximation[44] with the nonlocal gradient corrections of Becke[45] and Perdew.[46] The same methodology was applied to the NiSOD active site, where the initial atomic positions for the corresponding models were derived from X-ray crystallographic data.[5,6] The Cartesian coordinates for the DFT geometry-optimized models are available in the Supporting Information (Tables S3−S9). Vibrational frequency calculations were also performed with the ADF program on geometry-optimized models using the two-point differentiation method with ±0.01 Å displacements and integration constants of 5.0 or 6.0 (depending on the size of the molecule). With the exception of the [**3**$(MeCN)_2$] model (vide infra), only positive frequencies were obtained.[47]

All single-point DFT calculations were performed using the ORCA software package developed by Neese.[48] The computations were carried out within a spin-unrestricted formalism, using

(37) Teixeira, M.; Moura, I.; Xavier, A. V.; Dervartanian, D. V.; Legall, J.; Peck, H. D.; Huynh, B. H.; Moura, J. J. G. *Eur. J. Biochem.* **1983**, *130*, 481.
(38) Tanaka, H.; Yokoyama, A. *Chem. Pharm. Bull.* **1962**, *10*, 556.
(39) Yamamura, T.; Tadokoro, M.; Nakamura, N.; Tanaka, K.; Asakura, K. *Bull. Chem. Soc. Jpn.* **1990**, *63*, 999.
(40) Baerends, E. J.; Ellis, D. E.; Ros, P. *Chem. Phys.* **1973**, *2*, 41.
(41) Guerra, C. F.; Snijders, J. G.; te Velde, G.; Baerends, E. J. *Theor. Chem. Acc.* **1998**, *99*, 391.
(42) te Velde, G.; Baerends, E. J. *J. Comput. Phys.* **1992**, *99*, 84.
(43) Versluis, L.; Ziegler, T. *J. Chem. Phys.* **1988**, *88*, 322.
(44) Vosko, S. H.; Wilk, L.; Nusair, M. *Can. J. Phys.* **1980**, *58*, 1200.
(45) Becke, A. D. *J. Chem. Phys.* **1986**, *84*, 4524.
(46) Perdew, J. P. *Phys. Rev. B: Condens. Matter* **1986**, *33*, 8822.

Ahlrich's valence triple-ζ basis set (TZV)[49] with at least one set of polarization functions on all non-H atoms (the default in ORCA), along with the corresponding auxiliary basis set (TZV/C).[50,51] The calculations employed Becke's three-parameter hybrid functional[52,53] for exchange along with the Lee−Yang−Parr correlation functional[54] (B3LYP) and an integration grid of 4.0.[55] The gOpenMol program[56,57] developed by Laaksonen was used to generate isosurface plots of molecular orbitals (MOs) (using an isodensity value of 0.05 au).

Computed absorption spectra and EPR *g* values were also obtained with the ORCA program. These calculations employed the hybrid B3LYP functional, along with the basis sets described above for the single-point calculations. Electronic transition energies and dipole moments for all models were calculated with the time-dependent DFT (TD-DFT) method[58−60] within the Tamm−Dancoff approximation.[61,62] To increase computational efficiency, the resolution of the identity approximation[63] was used in calculating the Coulomb term. In each case, at least 40 excited states were calculated. EPR parameters were computed by solving the coupled-perturbed self-consistent-field (CP-SCF) equations.[64−66] The CP-SCF calculations of the **g** matrix included all orbitals within a ±100 hartree window of the highest occupied MO/lowest unoccupied MO energy gap, with the origin of the matrix defined by the center of electronic charge.

3. Results and Analysis

3.A.1. Spectroscopic Results for 1[Et$_4$N]. The deep-green color of complex **1** is the result of a broad absorption band that appears at 16400 cm^{-1} (ϵ = 3700 M^{-1} cm^{-1}) in the RT solution spectrum and at 15800 cm^{-1} in the solid-state spectrum measured at 10 K (Figure 1, top). Importantly, our solid-state MCD data reveal that the dominant absorption feature of **1** actually possesses contributions from two distinct transitions (bands II and III) that give rise to a derivative-shaped MCD feature centered at 15600 cm^{-1} (Figure 1, bottom). The observation of such a feature, commonly referred to as pseudo-***A*** terms, requires that the two transitions be differently polarized. Toward lower energy, a weak shoulder at ∼12400 cm^{-1}, referred to as band I, can be discerned in both the RT absorption spectrum and the low-temperature MCD spectra. On the basis of their energies and absorption intensities, we attribute bands I−III to S → Ni^{3+} charge-transfer (CT) transitions. The features to higher energy (above 18000 cm^{-1}) are assigned to ligand-based transitions since they also appear at similar energies in the absorption spectrum of the reduced [Ni^{2+}(pdtc)$_2$]$^{2-}$ complex.[34] Complex **1** exhibits an additional weak NIR absorption feature at 7900 cm^{-1} (not shown) that was assigned by Holm and Krüger to a Ni^{3+} ligand-field (LF) transition.[34] More specific band assignments based on our DFT studies of **1** are presented in the next section.

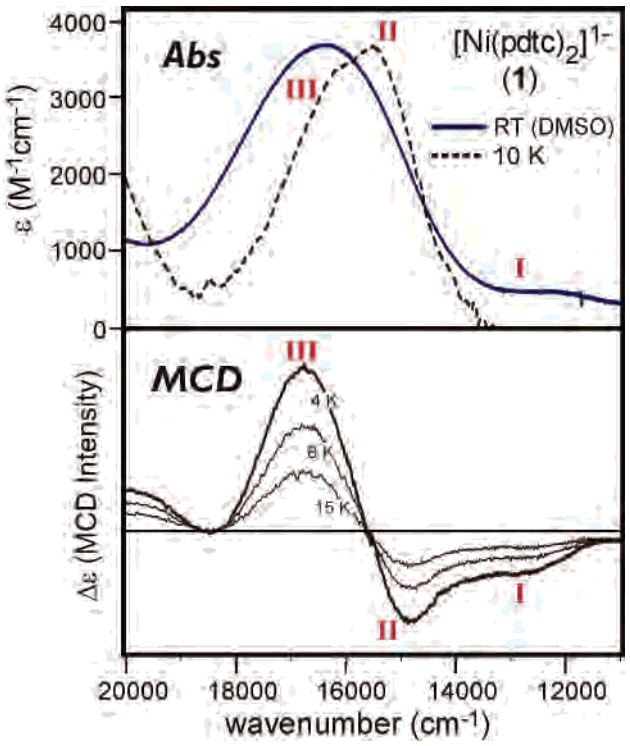

Figure 1. Top: Electronic absorption spectrum of complex **1** in DMSO at RT (solid line) and in the solid state at 10 K (dashed line). Bottom: Solid-state MCD spectra of **1** obtained with a magnetic field of 7 T at temperatures of 4, 8, and 15 K.

The solid-state rR spectrum of **1** obtained with 568 nm (17599 cm^{-1}) laser excitation (Figure 2) is dominated by two intense peaks at 171 and 247 cm^{-1} referred to as ν_1 and ν_2, respectively. With the exception of the peak at 364 cm^{-1} (ν_3), most of the weaker features observed to higher energy can be identified as overtone or combination bands of the ν_1 and ν_2 modes. The rR excitation profile data shown in Figure 3 reveal that both the 171 and 247 cm^{-1} peaks, as well as their combination band at 417 cm^{-1}, are strongly enhanced by excitation into the intense S → Ni^{3+} CT transitions of **1**, indicating that these peaks correspond to Ni−S stretching modes. By contrast, the 364 cm^{-1} feature exhibits only slight resonance enhancement in this region.

(47) Frequency calculations with the [**3**(MeCN)$_2$] model produced two imaginary modes at −11 and −15 cm^{-1} that arise from slight twisting motions of the axial MeCN ligands, along with a mode at −115 cm^{-1} that primarily involves the out-of-phase stretching motion of the two axial MeCN ligands. Because these imaginary modes only involve the axial ligands, they should have an insignificant effect on the DFT-computed frequencies for the normal modes associated with the [Ni(ema)] unit.
(48) Neese, F. *ORCA, an ab initio, density functional, and semiempirical program package*, version 2.4; Max-Planck Institut für Bioanorganische Chemie: Mülheim an der Ruhr, Germany, 2001.
(49) Schaefer, A.; Horn, H.; Ahlrichs, R. *J. Chem. Phys.* **1992**, *97*, 2571.
(50) Eichkorn, K.; Treutler, O.; Ohm, H.; Haser, M.; Ahlrichs, R. *Chem. Phys. Lett.* **1995**, *240*, 283.
(51) Eichkorn, K.; Weigend, F.; Treutler, O.; Ahlrichs, R. *Theor. Chem. Acc.* **1997**, *97*, 119.
(52) Becke, A. D. *J. Chem. Phys.* **1993**, *98*, 5648.
(53) Becke, A. D. *J. Chem. Phys.* **1993**, *98*, 1372.
(54) Lee, C. T.; Yang, W. T.; Parr, R. G. *Phys. Rev. B* **1988**, *37*, 785.
(55) The same basis sets and functionals for DFT geometry optimizations and single-point calculations were successfully employed in our earlier computational studies of NiSOD (see ref 8).
(56) Bergman, D. L.; Laaksonen, L.; Laaksonen, A. *J. Mol. Graphics Modell.* **1997**, *15*, 301.
(57) Laaksonen, L. *J. Mol. Graphics* **1992**, *10*, 33.
(58) Stratmann, R. E.; Scuseria, G. E.; Frisch, M. J. *J. Chem. Phys.* **1998**, *109*, 8218.
(59) Casida, M. E.; Jamorski, C.; Casida, K. C.; Salahub, D. R. *J. Chem. Phys.* **1998**, *108*, 4439.
(60) Bauernschmitt, R.; Ahlrichs, R. *Chem. Phys. Lett.* **1996**, *256*, 454.
(61) Hirata, S.; Head-Gordon, M. *Chem. Phys. Lett.* **1999**, *314*, 291.
(62) Hirata, S.; Head-Gordon, M. *Chem. Phys. Lett.* **1999**, *302*, 375.
(63) Neese, F.; Olbrich, G. *Chem. Phys. Lett.* **2002**, *362*, 170.
(64) Neese, F. *J. Chem. Phys.* **2003**, *118*, 3939.
(65) Neese, F. *Curr. Opin. Chem. Biol.* **2003**, *7*, 125.
(66) Neese, F. *J. Chem. Phys.* **2001**, *115*, 11080.

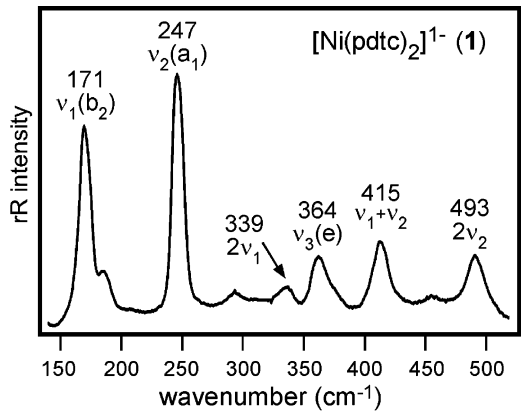

Figure 2. rR spectrum of **1** in the solid state obtained at 77 K using 568.2 nm (17599 cm^{-1}) laser excitation.

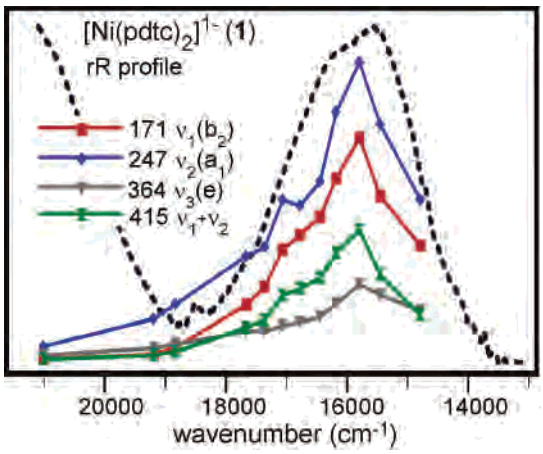

Figure 3. rR excitation profiles for the 171, 247, 364, and 415 cm^{-1} vibrational modes of **1** measured at 77 K with a solid-state sample. The corresponding 10 K absorption spectrum (broken line) is also shown for comparison.

To aid in our analysis of the vibrational features, we collected polarized rR spectra on frozen MeCN solutions of **1** at 77 K. As displayed in Figure S1 in the Supporting Information, the 247 cm^{-1} peak exhibits significant polarization ($I_\perp/I_\parallel = 0.18$) and can thus be assigned to a totally symmetric mode, whereas the weakly polarized 171 cm^{-1} peak ($I_\perp/I_\parallel = 0.86$) must arise from a nontotally symmetric mode.[67] This latter assignment may initially appear to conflict with the rR profiles discussed above because only totally symmetric modes can experience resonance enhancement via the conventional A-term mechanism[67] (not to be confused with the ***A*** terms discussed above for MCD spectroscopy). To resolve this apparent contradiction, the unusual manner in which the 171 cm^{-1} peak acquires rR enhancement is explored in the next section.

3.A.2. Computational Analysis for 1[Et$_4$N]. The structure of our DFT geometry-optimized model of complex **1** agrees nicely with the crystallographically derived structure reported by Holm and Kruger,[34] which exhibits approximate D_{2d} symmetry (Table S1 in the Supporting Information). A single-point DFT calculation on this model provided the MO diagram shown in Figure 4, which highlights key features of the electronic structure of complex **1**. The unpaired electron of **1** resides in the Ni^{3+} z^2-based MO (#114), which is consistent with the fact that $g_\perp > g_\parallel \approx g_e$ in the corresponding EPR spectrum ($g_\perp = 2.14$ and $g_\parallel = 2.04$).[34] The unoccupied Ni x^2-y^2-based MO (#115) is comprised of nearly equal amounts of Ni 3d (46%) and S 3p (48%) orbital character, indicating the presence of strong, highly covalent σ interactions between the Ni^{3+} center and the S ligands. Interestingly, the highest-energy occupied MOs are predominately S 3p-based, lying well above the three occupied Ni 3d-based MOs that constitute the t_{2g} set in the parent O_h symmetry (i.e., the *xz*-, *yz*-, and *xy*-based MOs). A similar "partially inverted" MO energy ordering was found for the NiSOD active site, with the MO energies following the order Ni(e_g) > S(π/σ) > Ni(t_{2g}).[8]

With the goal of obtaining more precise assignments for the salient features in our spectroscopic data, the absorption spectrum of complex **1** was calculated using the TD-DFT method, which provides transition energies and intensities as well as information about the donor and acceptor orbitals for each calculated transition. TD-DFT predicts an intense S → Ni^{3+} CT transition at 14114 cm^{-1} ($\epsilon = 3000$ M^{-1} cm^{-1}; see Figure S2 in the Supporting Information) that undoubtedly corresponds to the experimentally observed feature at ~16000 cm^{-1} (Figure 1). Our TD-DFT results predict further that this band is due to the MO #111/112(e) → 115(b_2) transition, which possesses *x*/*y* polarization due to the 2-fold degeneracy of the donor MO (Figure 4). Thus, our TD-DFT computations indicate that bands II and III are the *x*- and *y*-polarized components of a single e → b_2 parent transition, an assignment that is fully supported by the fact that these bands give rise to a pseudo-***A*** term feature in the MCD spectrum of **1** (Figure 1, bottom). Furthermore, our computational data suggest that band I corresponds to the 113(a_2) → 115(b_2) Ni^{3+} LF transition, which has a calculated energy of 11352 cm^{-1} (Figure 4). Although this transition is formally symmetry-forbidden, its low absorption intensity observed experimentally likely arises from static distortions and/or vibronic coupling (i.e., Herzberg−Teller coupling). Finally, in agreement with our qualitative assignments provided above, the TD-DFT calculation for **1** predicts that nearly all features above 20000 cm^{-1} arise from ligand-based transitions and yields an energy of 9584 cm^{-1} for the Ni(z^2) → Ni(x^2-y^2) LF band (Figure S2 in the Supporting Information), in reasonable agreement with the experimental value of 7900 cm^{-1}.[33]

As shown in Figure 5, the four Ni−S stretching modes of **1**, ν(Ni−S), transform as $a_1 + b_2 + e$ in D_{2d} symmetry, and previous studies on similar complexes[68,69] revealed an energy ordering of $\nu(b_2) < \nu(a_1) < \nu(e)$. On the basis of these results and the rR polarization data mentioned above, we assign the 171 cm^{-1} peak (ν_1) to the ν(Ni−S) mode of b_2 symmetry and the 247 cm^{-1} peak (ν_2) to the totally symmetric

(67) Czernuszewicz, R. S.; Spiro, T. G. In *Inorganic Electronic Structure and Spectroscopy*; Solomon, E. I., Lever, A. B. P., Eds.; Wiley-Interscience: New York, 1999; Vol. 1, pp 353−442.

(68) Nakamoto, K. *Infrared and Raman Spectra of Inorganic and Coordination Compounds*, 4th ed.; Wiley-Interscience: New York, 1986.

(69) Huang, Y. H.; Moura, I.; Moura, J. J. G.; Legall, J.; Park, J. B.; Adams, M. W. W.; Johnson, M. K. *Inorg. Chem.* **1993**, *32*, 406.

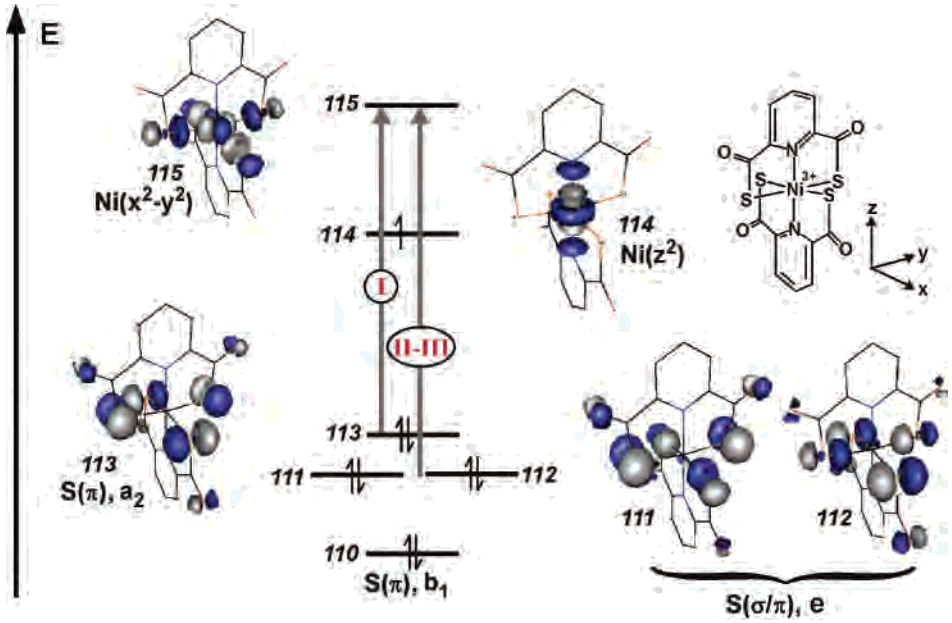

Figure 4. Qualitative MO energy-level diagram and isosurface plots obtained from a DFT calculation for complex **1**. The one-electron excitations producing the major contributions to the transitions responsible for bands I−III (as provided by TD-DFT calculations) are also indicated.

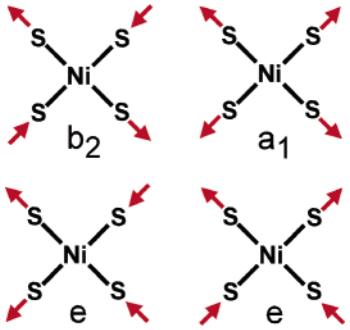

Figure 5. Schematic depiction of the ν(Ni−S) normal modes of complex **1**.

Table 1. Comparison of Experimental and DFT-Calculated Vibrational Frequencies for Complex **1**

mode	exptl ν (cm^{-1})	calcd ν (cm^{-1})	Δ^a (cm^{-1})	Δ^b (%)	symmetry
ν_1(Ni−S)	171	163	−8	−5	b_2
ν_2(Ni−S)	247	226	−21	−9	a_1
ν_3(Ni−S)	364	343	−21	−6	e

[a] Absolute difference between DFT-calculated and experimental frequencies. [b] Same as footnote *a* but in relative units.

ν(Ni−S) mode (Figure 2). The peak at 364 cm^{-1} is then assigned to the doubly degenerate ν(Ni−S) mode of e symmetry, consistent with the lack of rR enhancement observed for this feature. In support of these assignments, our DFT-computed vibrational frequencies for **1** fall within 10% of the experimental values (Table 1).

In order to quantify the strength of the Ni−S bonding interactions in **1**, a NCA of the rR data was performed using a general valence force field. The large size of the molecule required the use of a simplified model that consisted solely of the [NiS_4] unit and the α-C atoms of the pdtc ligand. By systematically adjusting the force field to fit the experimental frequencies, we arrived at a value of f(Ni−S) = 1.08 mdyn $Å^{-1}$ for the Ni−S stretching force constant. A survey of the literature suggests that M−S stretching force constants generally fall within the range of 1.2−1.8 mdyn $Å^{-1}$; thus, our NCA results indicate that the Ni^{3+}−S bonds in complex **1** are unusually weak. This conclusion is consistent with the fact that these bonds are significantly longer in **1** than in other Ni−S complexes (2.28 vs ∼2.18 Å, respectively).[33,34]

Our DFT and NCA results can now be used to explore the origin of the strong resonance enhancement of the 171 cm^{-1} vibrational mode of b_2 symmetry in the rR spectrum of **1**. As noted above, the dominant absorption band of **1** is due to an e → b_2 excitation; hence, the corresponding excited state is 2-fold orbitally degenerate. According to the Jahn−Teller theorem, this excited-state degeneracy is removed by distorting the molecule along the nontotally symmetric b_2 mode. This distortion allows the b_2 mode to couple to the e → b_2 electronic transition and leads to enhancement of the corresponding Raman peak at 171 cm^{-1} via the conventional A-term mechanism. The electronic origin of the molecular distortion along the b_2 mode can be discerned from the compositions of the donor MOs of e symmetry (MOs #111 and #112), which exhibit Ni−S σ-bonding interactions along one S−Ni−S axis and π-bonding interactions along the perpendicular axis (Figure 4). Given that the Ni(x^2-y^2) orbital (MO #115) participates exclusively in σ-antibonding interactions, excitation from MO #111 to MO #115 causes a lengthening of the Ni−S bonds along the x axis while simultaneously encouraging the Ni−S bonds along the y axis to contract. Exactly the opposite scenario occurs if MO #112 serves as the donor orbital. Hence, on the basis of this MO analysis, the molecular distortions accompanying the e → b_2 excitation are indeed expected to closely match the nuclear displacements associated with the b_2 mode.

3.B.1. Spectroscopic Results for 2. Oxidation of $[Ni^{2+}(emb)]^{2-}$ (**2**^{red}) with I_2 in DMF at RT results in the formation of the bright-green Ni^{3+} complex **2**, which is characterized by an intense absorption feature (band i in Figure

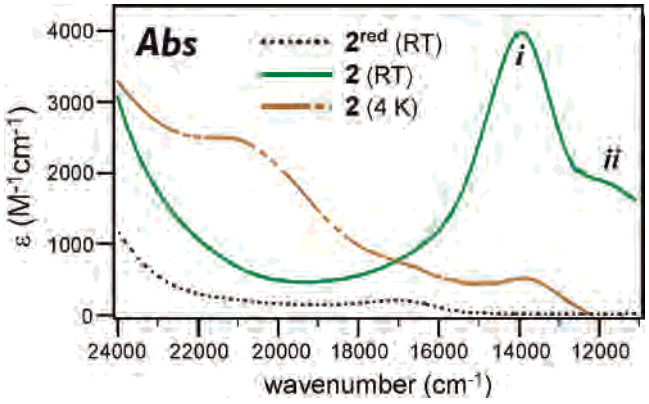

Figure 6. Electronic absorption spectra of complex $\mathbf{2}^{red}$ (dotted black line) and **2** (solid green line) in DMF at RT, along with the low-temperature (4 K) spectrum of **2** in a 1:1 mixture of propionitrile/butyronitrile.

6) at 14000 cm^{-1} with $\epsilon \approx 4000$ M^{-1} cm^{-1}. A shoulder of lower intensity (band ii) is also evident at ~12000 cm^{-1}. Interestingly, complex **2** exhibits *thermochromism* in all of the solvents we examined, dramatically changing its color from green to brown upon sample cooling. Accordingly, as shown in Figure 6, the low-temperature (4 K) absorption spectrum of **2** in a 1:1 mixture of propionitrile/butyronitrile is strikingly different from the RT spectrum, with the dominant band at 14000 cm^{-1} replaced by a series of weaker absorption features to higher energy. However, this thermochromic behavior is only evident at higher concentrations of **2** (>~1 mM), as more dilute solutions retain their green color upon freezing.

Significantly, low-temperature MCD spectra obtained for "brown" samples of **2** exhibit only weak, temperature-independent features (Figure S3 in the Supporting Information), indicating that the brown species is diamagnetic. This conclusion is further supported by the fact that brown solutions of **2** are essentially EPR-silent. However, despite its overall diamagnetism, our results clearly indicate that the brown species is comprised of Ni^{3+} centers because the addition of small amounts of pyridine to these samples resulted in the development of a strong EPR signal with $g = 2.34$, 2.27, and 2.01 (Figure S4 in the Supporting Information). This spectrum is identical with the one published by Holm and Kruger for the monomeric complex $[Ni^{3+}(emb)(py)]^-$ (**2-py**).[35] Importantly, the MCD spectra obtained for a dilute sample of **2**, which retained its green color at low temperatures, exhibit a band with a maximum at 13600 cm^{-1} (Figure S5 in the Supporting Information) that corresponds to the dominant absorption feature observed at RT (Figure 6). In this case, all MCD features are temperature-dependent, indicating that the green species is paramagnetic.

Collectively, the data presented here indicate that **2**, a green-colored monomeric species with $S = {}^1/_2$ at RT, has a tendency to dimerize at low temperatures and high concentrations, thereby forming the brown complex $[\mathbf{2}]_2$. Pyridine inhibits dimer formation by coordinating to the Ni^{3+} center as an axial ligand to give the monomeric species **2-py**. Interestingly, the ability of such $[Ni^{3+}S_2N_2]$ complexes to dimerize at reduced temperatures was first noted by Holm and Kruger in their studies of **3**, which, similar to **2**, acquires

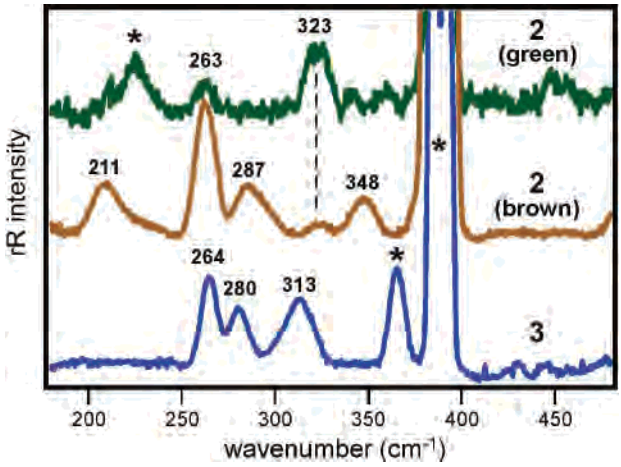

Figure 7. Top and middle: rR spectra of "green" and "brown" samples of **2**, respectively, obtained with 752.5 nm (13290 cm^{-1}) laser excitation. Bottom: rR spectrum of **3** collected with 647.1 nm (15450 cm^{-1}) excitation. All spectra were obtained at 77 K on frozen MeCN solutions. Peaks arising from the MeCN solvent and I_x overtones are indicated with asterisks.

a reddish color in its dimerized form.[33] They did not report similar dimerization behavior for **2**, however, as their studies of this complex were conducted at sufficiently low concentrations to retain the monomer structure.[35]

The thermochromism of **2** is also evident from the very different rR spectra obtained for brown and green samples of this species, as shown in Figure 7. Both spectra were acquired at 77 K on frozen MeCN solutions using a 753 nm (13300 cm^{-1}) laser excitation. The green species exhibits two sample-derived features at 263 and 323 cm^{-1}, while the brown species displays peaks at 211, 263, 287, and 348 cm^{-1} (the peak at 226 cm^{-1} is an overtone of an I_x-derived peak). Interestingly, the 323 cm^{-1} peak of the green species also appears weakly in the spectrum of the dimer $[\mathbf{2}]_2$, indicating that the latter sample also contained a small amount of the monomer **2**. This result is consistent with our EPR data obtained for the brown species, which exhibits a faint $S = {}^1/_2$ signal with g values identical with those reported previously for **2** ($g = 2.29$, 2.11, and 2.04).[35]

3.B.2. Computational Analysis for 2. DFT geometry optimizations carried out by imposing a planar C_{2v} symmetry on the monomer **2** yielded reasonable $Ni^{3+}-S$ and $Ni^{3+}-N$ bond lengths of 2.18 and 1.89 Å, respectively (Table S1 in the Supporting Information). Analysis of the resulting electronic structure reveals that the unpaired electron of **2** resides in the Ni(xz)-based orbital of π symmetry (Figure 8) rather than the Ni(z^2)-based MO, as in the case of the six-coordinate **1**. This singly occupied MO (SOMO) is composed of 48% Ni, 22% S, and 13% N orbital character (Table S2 in the Supporting Information), indicating that the $Ni^{3+}-$ligand bonding interactions in **2** are similarly covalent as in complex **1**. The fact that the SOMO of **2** has π symmetry also accounts for the highly rhombic EPR spectrum observed experimentally for this species, which is nicely reproduced by our DFT g-value calculations (Table 2). The more axial **g** tensor of **2-py** is due to the fact that pyridine coordination to the Ni^{3+} center causes a sufficiently large destabilization of the Ni(z^2)-based MO to render this orbital the new SOMO. Given this electronic structure description, it is not surprising

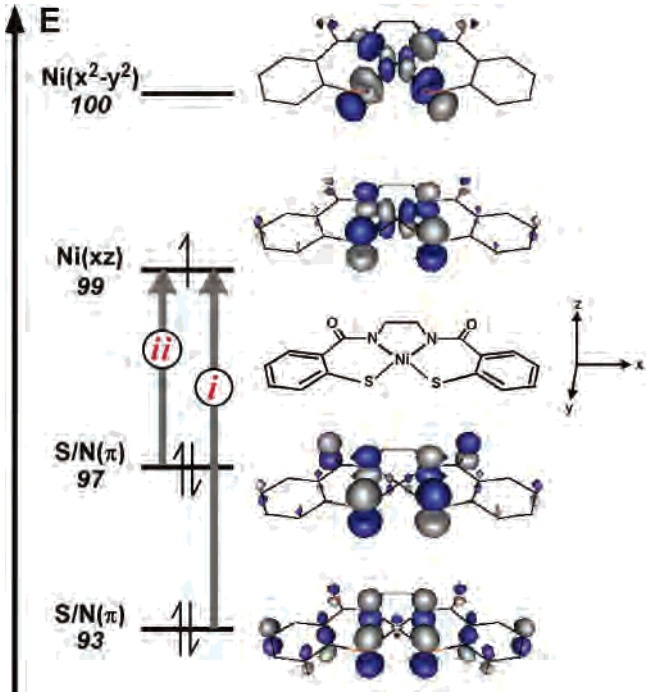

Figure 8. Qualitative MO energy-level diagram and isosurface plots obtained from a DFT calculation of complex **2**. The electronic excitations corresponding to bands i and ii (as provided by TD-DFT calculations) are also indicated.

Table 2. Comparison of Experimental and DFT-Calculated g Values for Various Species of Complexes **2** and **3**

model	method	g_x	g_y	g_z
2	DFT	2.25	2.11	2.06
	exptl	2.29	2.11	2.04
3	DFT	2.50	2.33	2.06
[**3**(MeCN)]	DFT	2.24	2.23	2.04
[**3**(MeCN)$_2$]	DFT	2.23	2.22	2.04
	exptl	2.23	2.18	2.01

that our TD-DFT calculations attribute the dominant absorption features of **2**, bands i and ii, to the S/N(π) → Ni^{3+}(d_π*) transitions shown in Figure 8. The computed energies of 14450 and 9200 cm^{-1} for bands i and ii, respectively, are in reasonable agreement with the experimental values of 14000 and 12000 cm^{-1}.

Our DFT results also aid in the interpretation of the experimental rR spectrum of the monomeric form of **2**, which is dominated by a feature at 323 cm^{-1} (Figure 7). Given that this spectrum was obtained by laser excitation into an absorption band with S/N → Ni^{3+} CT character, it is straightforward to attribute the 323 cm^{-1} feature to the totally symmetric breathing mode of the [$Ni^{3+}S_2N_2$] core (Figure 9). This assignment is corroborated by DFT frequency calculations that provide an energy of 339 cm^{-1} for this mode. Moreover, because the predicted frequency of the antisymmetric ν(Ni−S/N) stretching mode shown in Figure 9 is 278 cm^{-1}, we tentatively assign the experimentally observed peak at 264 cm^{-1} to this vibration (Figure 7).

As noted in the previous section, **2** has a tendency to dimerize at low temperatures to yield the brown diamagnetic species [**2**]$_2$ with absorption and rR spectra distinct from those of the monomeric form. Figure 10 illustrates the three most viable structures, labeled A−C, for [**2**]$_2$. In model A,

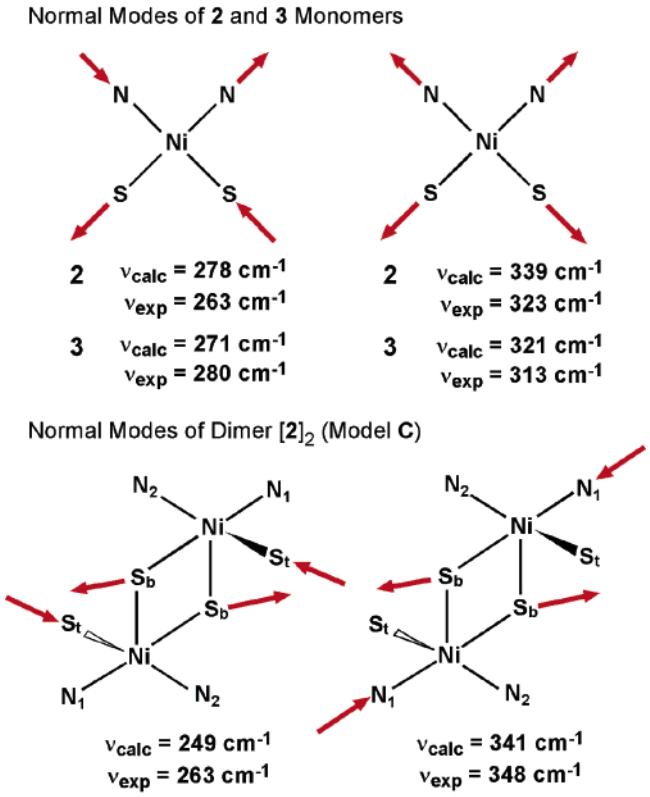

Figure 9. Schematic depictions of select Ni−S/N stretching normal modes of the monomers **2** and **3** (top) and the dimer [**2**]$_2$ (bottom). Experimental and DFT-computed frequencies for the respective modes are also indicated.

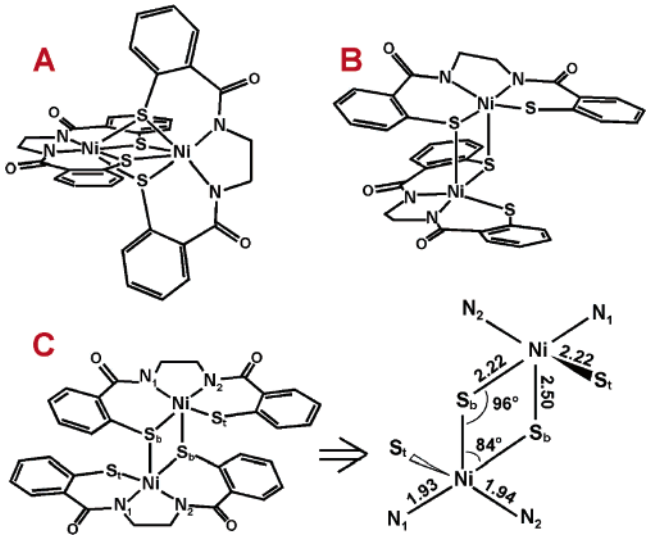

Figure 10. Viable models A−C of the dimer [**2**]$_2$. Core structural parameters for the DFT-optimized model C are provided at the bottom right.

the planes of the two [Ni(emb)]$^-$ monomers are oriented perpendicular to each other to permit the formation of a [Ni_2(μ-SR)$_4$] core with four bridging S ligands (S_b), whereas models B and C feature "stacked" (or lateral) orientations in which the emb planes are aligned in a parallel fashion, resulting in Ni_2 units with two bridging S ligands. The latter two models differ with respect to their overall symmetries: C_2 for B and C_i for C.

DFT geometry optimizations carried out for these three models indicate that structure A is not energetically viable

because it rapidly dissociates into its two monomeric units. In contrast, optimization of models B and C provided two stable species that have nearly identical metric parameters and total energies. Thus, it is likely that $[\mathbf{2}]_2$ adopts a lateral conformation in solution, although our computations cannot determine whether B or C is more favorable. However, since the presence of an inversion center simplifies the analysis of the vibrational modes and electronic structure, the remainder of this paper will focus on model C, whose core structural parameters are listed in Figure 10. An interesting feature of C is that the axial $Ni^{3+}-S_b$ bonds of the $[Ni_2(\mu\text{-}S_b)_2]$ core are rather long (2.50 Å), while the equatorial $Ni^{3+}-S$ and $Ni^{3+}-N$ bond distances are within ~0.04 Å of those found in the monomeric structure of **2**. The most significant structural change upon dimerization is the movement of the two nonbridging S atoms (S_t) out of the $[NiS_bN_2]$ plane by 27°, resulting in distorted square-pyramidal coordination environments for the two Ni^{3+} centers ($\tau = 34°$).[70]

The spectroscopic parameters obtained in additional DFT computations on model C agree nicely with those found experimentally for the $[\mathbf{2}]_2$ dimer. As shown in Figure S6 in the Supporting Information, TD-DFT calculations on a truncated[71] model of C predict that dimerization of the monomer **2** shifts the prominent S/N → Ni^{3+} CT transitions to higher energies and reduces their intensities, in excellent agreement with our experimental absorption data. These spectral changes reflect key differences in the electronic structures of the monomer and dimer species. While in **2** the single unpaired electron resides in the Ni(*xz*)-based MO, the magnetic orbitals of the dimer are the Ni(z^2)-based MOs that exhibit poor overlap with the S and N π-donor orbitals. Thus, the corresponding CT transitions carry lower absorption intensities than those in the monomer species and are blue-shifted because of destabilization of the Ni(z^2)-based acceptor MOs by the axial thiolate ligands.

On the basis of previous studies of $[M_2(\mu\text{-}S)_2]$ complexes,[72] the $[\mathbf{2}]_2$ dimer is expected to exhibit intense rR features associated with the breathing modes of the Ni_2 core (Figure 9). Our DFT frequency calculations for the truncated model C predict two such modes at 341 and 249 cm^{-1} that likely correspond to the experimentally observed peaks at 348 and 263 cm^{-1}, respectively, although the 287 cm^{-1} feature (Figure 7) is another possible candidate for the lower-frequency mode. Importantly, both of the computed modes are Raman active since they are symmetric with respect to the inversion center of model C. The large frequency difference between these two modes is due to different coupling interactions with the remaining $Ni^{3+}-S/N$ stretching motions. For instance, our calculations indicate that the $Ni^{3+}-S_b$ and $Ni^{3+}-S_t$ stretching motions in the 249 cm^{-1} mode are strongly coupled in an antisymmetric fashion, as shown in Figure 9. It is therefore not surprising that this mode possesses an experimental energy similar to that of the corresponding mode of the monomer **2**. In contrast, the higher-energy mode predicted at 341 cm^{-1} primarily consists of antisymmetric combinations of the $Ni^{3+}-S_b$ and $Ni^{3+}-N_1$ stretching motions, where N_1 lies trans to the S_b ligand (Figure 9). Finally, the peak at 211 cm^{-1} in the rR spectrum of $[\mathbf{2}]_2$ likely arises from the axial $\nu(Ni-S_b)$ stretching mode for which our DFT calculation predicts a frequency of 219 cm^{-1}. Thus, our studies suggest that the appearance of a feature at ~210 cm^{-1} in the rR spectra of $[Ni^{3+}S_2N_2]$ complexes is diagnostic for dimer formation, given that the monomeric species do not exhibit any vibrational features in this frequency range.

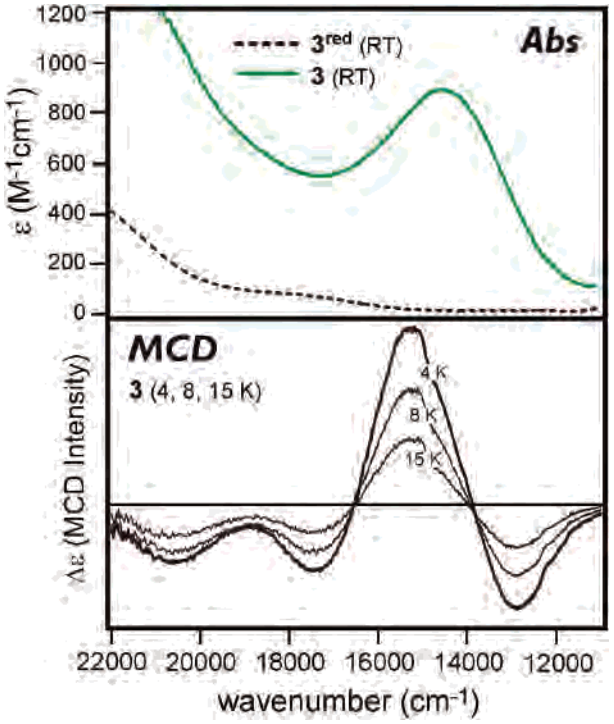

Figure 11. Top: Electronic absorption spectrum of complexes $\mathbf{3}^{red}$ (dashed line) and **3** (solid line) in DMSO at RT. Bottom: MCD spectra of **3** in a 1:1:1 mixture of MeCN/propionitrile/butyronitrile measured with a magnetic field of 7 T at temperatures of 4, 8, and 15 K.

3.C.1. Spectroscopic Results for 3. Dark-green solutions of **3** were generated by treatment of $[Ni^{2+}(ema)]^{2-}$ ($\mathbf{3}^{red}$) with I_2 in various aprotic solvents. The absorption spectra of the resulting species exhibit a prominent band at ~14600 cm^{-1} with an ϵ value of ~1000 M^{-1} cm^{-1} (Figure 11, top). On the basis of our studies of **1** and **2** described above, this feature is readily assigned to a S/N → Ni^{3+} CT transition. Importantly, the green color of these solutions was retained upon freezing, suggesting that the monomer **3** does not dimerize under the conditions employed in this study. This conclusion is confirmed by the low-temperature EPR spectrum of **3** (Figure S4 in the Supporting Information), which is clearly indicative of a Ni^{3+} species with $S = {}^1/_2$ (the experimental *g* values of 2.23, 2.18, and 2.01 are identical with those reported previously[33]). Moreover, the low-temperature absorption spectrum of **3** (not shown) closely

(70) The geometric parameter τ is defined as $\tau = |(\beta - \alpha)|/60$, where α and β are the two trans basal angles in pseudo-square-pyramidal geometry. In idealized square-pyramidal geometries, $\alpha = \beta$, but trigonal distortions result in $\alpha \neq \beta$.

(71) Because of the large size of the dimer complex, these calculations employed a truncated model of C in which the ethylene bridges were removed and the phenyl rings of the emb ligand were replaced by C=C bonds.

(72) Que, L.; Tolman, W. B. *Angew. Chem., Int. Ed.* **2002**, *41*, 1114.

Table 3. Experimental, DFT-Calculated, and NCA-Predicted Vibrational Frequencies, along with PEDs and Relevant Force Constants for the Monomers **2** and **3**

complex	mode	exptl[a] ν (cm^{-1})	DFT[b] ν (cm^{-1})	NCA ν (cm^{-1})	PEDs[c]	force constants[c] (mdyn $Å^{-1}$)
2	1	263	278	265	55% Ni−S, 44% Ni−N	f(Ni−S) = 1.59
	2	323	339	321	46% Ni−S, 53% Ni−N	f(Ni−N) = 1.21
	3		375	377	45% Ni−S, 45% Ni−N	
	4		435	434	55% Ni−S, 44% Ni−N	
3	1	280	271	278	69% Ni−S, 31% Ni−N	f(Ni−S) = 1.51
	2	313	321	312	50% Ni−S, 49% Ni−N	f(Ni−N) = 1.28
	3		391	392	32% Ni−S, 67% Ni−N	
	4		421	421	51% Ni−S, 47% Ni−N	

[a] Frequency derived from rR data. [b] Frequency derived DFT calculation. [c] PEDs and force constants obtained from NCAs (1 mdyn $Å^{-1}$ = 100 N/m).

resembles the RT spectrum, and the features in the corresponding MCD spectrum display temperature-dependent behavior (Figure 11, bottom), as expected for a paramagnetic species. Collectively, our spectral data clearly indicate that **3** retains its monomeric structure even at low temperatures.

The rR spectrum of **3** (Figure 7) exhibits two intense features at 264 and 313 cm^{-1} that are both enhanced by laser excitation into the dominant absorption feature of this species. In contrast, the weaker peak at 280 cm^{-1} experiences only minor resonance enhancement, suggesting that it arises from a nontotally symmetric normal mode. Given their structural similarities, it is not surprising that the rR spectrum of **3** resembles that of the monomeric form of **2**, with both spectra exhibiting an intense peak near 320 cm^{-1} along with a weaker feature in the vicinity of 270 cm^{-1}. In the previous section, we demonstrated for **2** that these peaks correspond to the symmetric and antisymmetric $\nu(Ni^{3+}-S/N)$ modes, respectively, shown in Figure 9, and it is reasonable to make analogous assignments for the spectrum of **3**. These assignments are corroborated by the DFT frequency calculations and NCA for **3** presented below.

3.C.2. Computational Analysis for 3. Our spectroscopic results clearly indicate that the mononuclear forms of **2** and **3** have fundamentally different electronic structures. As we showed above, the Ni(π*) character of the SOMO of **2** results in a highly rhombic **g** tensor and intense, low-energy S/N(π) → $Ni^{3+}(\pi^*)$ transitions. In contrast, **3** exhibits a nearly axial EPR spectrum, with the g_z value near the free-electron value of 2.002 characteristic of a $S = {}^1/_2$ system in which the unpaired electron resides in the Ni(z^2)-based MO. Additionally, the modest intensities of the S/N → Ni^{3+} CT features in the absorption spectrum of **3**, as compared to those in the spectrum of **2**, are also indicative of a Ni(z^2)-based SOMO. This latter conclusion is based on the same orbital overlap considerations employed above to rationalize the decrease in the absorption intensity upon dimerization of **2** to yield $[\mathbf{2}]_2$.

Although the experimental data conclusively demonstrate that **3** possesses a Ni(z^2)-based SOMO, our DFT computations for this species invariably predicted the single unpaired electron to reside in the Ni(xz)-based MO (Figure S7 in the Supporting Information), resulting in an electronic structure nearly analogous to the one computed for **2**. This ground-state configuration was obtained regardless of what functional or basis sets were utilized in the DFT calculations, and inclusion of solvation effects with the conductor-like screening model (COSMO)[73,74] also failed to yield the correct description of the SOMO of **3**. Consequently, DFT predicts highly rhombic g values for **3**, in obvious disagreement with the axial EPR spectrum observed experimentally (Table 2).

In order to obtain an electronic structure consistent with the spectroscopic data, we explicitly included solvent molecules in our subsequent computational models of **3**. The geometry-optimized models [**3**(MeCN)] and [**3**$(MeCN)_2$] feature one and two MeCN ligands, respectively, coordinated to the axial positions of the Ni^{3+} center, and the computed wave functions for both species correctly place the unpaired electron in Ni(z^2)-based MOs (Figure S7 in the Supporting Information). Moreover, the calculated g values for these solvent-bound models closely match the experimental values (Table 2), indicating that both provide adequate descriptions of the electronic structure of **3** in solution. The remainder of this study will focus on the [**3**$(MeCN)_2$] model because it preserves the planarity of the $[Ni^{3+}S_2N_2]$ unit and yields g values that agree slightly better with the experimental data. Moreover, as indicated in Figure 9, DFT calculations for the [**3**$(MeCN)_2$] model predict frequencies of 268 and 315 cm^{-1} for the symmetric and antisymmetric Ni−S/N stretching modes, respectively, in remarkable agreement with our experimental data. These computations suggest further that the intense peak at 264 cm^{-1} arises from a symmetric mode that has primarily N−Ni−N and S−Ni−S bending character.

Using the DFT-assisted rR spectral assignments and the vibrational frequencies provided in Figure 9, we performed a generalized NCA for the $[Ni^{3+}S_2N_2]$ species using a suitably truncated model. Because experimental frequencies are only available for two of the four Ni−S/N stretching modes, the frequencies of the remaining two modes (which correspond to the "e" modes in Figure 5) were taken from our DFT frequency calculations of **2** and **3**. Systematic adjustment of the force fields for **2** and **3** resulted in the NCA-computed frequencies and potential energy distributions (PEDs) shown in Table 3. Most importantly, this analysis yields force constants of ~1.55 and 1.25 mdyn $Å^{-1}$ for the Ni−S and Ni−N stretching motions, respectively (Table 3). Thus, the Ni−ligand bonding interactions in the four-coordinate models (**2** and **3**) are considerably stronger than those in the six-coordinate complex **1**.

(73) Klamt, A.; Jonas, V.; Burger, T.; Lohrenz, J. C. W. *J. Phys. Chem. A* **1998**, *102*, 5074.
(74) Klamt, A.; Schuurmann, G. *J. Chem. Soc., Perkin Trans.* **1993**, *2*, 799.

4. Discussion

Given the importance of S ligation in redox-active Ni enzymes in general, and in NiSOD catalysis in particular, we have sought to advance our understanding of Ni−S bonding interactions through examination of three Ni^{3+}-containing model complexes, **1**−**3**. The electronic absorption spectra of these models are dominated by intense S → Ni^{3+} CT transitions in the visible regions (Figures 1, 6, and 11). Consequently, laser excitation into these bands yields rR spectra that are dominated by vibrational modes predominately involving Ni−S stretching motions. To probe the ground-state magnetic properties of these models, we also carried out EPR and MCD experiments. These experimental data were interpreted with the aid of DFT calculations that were used to compute absorption spectra, EPR *g* values, and vibrational frequencies. This combined spectroscopic/computational approach permitted detailed assignments of the key features in the absorption and rR spectra of **1**−**3** and also allowed us to discriminate between viable structural models for the dimeric form of complex **2**.

While substantial structural and electronic differences exist among complexes **1**−**3**, a common feature is the presence of highly covalent Ni−S/N σ-bonding interactions, as demonstrated by the fact that the Ni(x^2-y^2)-based MOs of all three complexes contain roughly equal amounts of Ni and ligand orbital character. This exceptional degree of covalency derives from the energetic proximity of the Ni d orbitals and the S p-based lone pairs,[75] which is particularly evident from the DFT-computed bonding scheme for complex **1** (Figure 4), where the ligand-based MOs lie energetically between the "e_g" and "t_{2g}" sets of Ni d-based MOs. Moreover, the substantial amount of ligand orbital character in the SOMO of **2** (52%) suggests that the emb ligand is partially oxidized along with the Ni center in the $\mathbf{2^{red}} \rightarrow \mathbf{2}$ conversion, further highlighting the covalent nature of the Ni−ligand bonds in these models.

Our spectroscopic studies reveal that the excited state associated with the dominant S → Ni^{3+} CT transition of **1** is subject to a Jahn−Teller distortion, which is manifested in the resonance enhancement of the ν(Ni−S) mode of b_2 symmetry at 171 cm^{-1}. Quantitative analysis of the rR data indicates that the Ni^{3+}−S bonds in **1**, while quite covalent, are dramatically weaker ($f_{Ni-S} = 1.08$ mdyn $Å^{-1}$) than those found in **2** or **3** ($f_{Ni-S} \approx 1.55$ mdyn $Å^{-1}$). This result suggests that thiocarboxylate ligands of **1** are poor donors compared to thiolate ligands of **2** and **3**, although the greater coordination number of **1** also causes an additional weakening of the equatorial bonds.

Given the structural similarities between **2** and **3**, it is remarkable that the spectroscopic data obtained for these four-coordinate complexes point to substantial differences in their electronic structures. Our DFT calculations indicate that the unpaired electron of **2** resides in the Ni(*xz*)-based MO, in accordance with the rhombic EPR spectrum displayed by this species. This electron configuration allows for the formation of strong π-bonding interactions between the Ni center and the S/N ligand set, which are reflected in the intense S/N(π) → Ni^{3+}(π^*) CT transitions that appear in the corresponding absorption spectrum (Figure 6). In contrast, the nearly axial EPR spectrum of complex **3** requires a Ni(z^2)-based SOMO, consistent with our DFT *g*-value calculations for this species. The change in the ground-state character is also reflected in the diminished absorption intensity of the S/N → Ni^{3+} CT transitions observed for **3** (Figure 11).

Collectively, these results suggest that, in four-coordinate [$Ni^{3+}S_2N_2$] complexes, the Ni z^2-, *xz*-, and *yz*-based MOs are in close energetic proximity, such that subtle differences in ligand properties and/or solvent effects can alter the identity of the SOMO. Indeed, our DFT calculations for **2** and **3** indicate that both complexes would, in fact, favor Ni(π*)-based SOMOs in the gas phase, implying that solvent interactions play an important role in tuning the electronic structure. Another possible explanation for the different SOMOs of **2** and **3** lies in the differing values of the Ni−S−C_α angles, since the σ-donating ability of thiolate ligands is maximized when $\angle$Ni−S−$C_\alpha = 90°$.[76] Thus, the comparatively wide angle of 114° computed for **2** is expected to stabilize the Ni(z^2) orbital relative to the Ni(*xz*) orbital, perhaps accounting for the observed Ni d-orbital splitting pattern. The more acute value of 97° found for **3** likely mitigates this effect. Regardless of its origin, the change in the ground-state wave function from **2** to **3** has major electronic-structure implications because the S and N donors of **2** can participate in σ *and* π interactions with the Ni^{3+} center, whereas only σ interactions are possible in **3**. Thus, the Ni^{3+}−S bonds are stronger in **2** than in **3**, even though previous studies have demonstrated that aryl thiolates tend to form weaker metal−S bonds than alkyl thiolates.[69,77] It is also interesting to note that our DFT calculations overestimate frequencies of the Ni−S/N stretching modes of **2** by ∼5%, whereas the corresponding frequencies for **1** and **3** are generally underestimated by nearly the same amount (Table 1 and Figure 9). This result suggests that DFT somewhat overestimates the strength of π-bonding interactions relative to σ-bonding interactions, a deficiency that has been noted in previous computational studies of transition-metal complexes.[78,79]

Our experimental data indicate that complex **2**, while a green-colored monomer at RT, exists as a brown-colored dimer at high concentrations and low temperatures. Characterization of $[\mathbf{2}]_2$ with MCD and EPR spectroscopies revealed that this dimer species has a diamagnetic ground state due to antiferromagnetic coupling between the two Ni^{3+} centers. Three potential structures for $[\mathbf{2}]_2$ (A−C) were evaluated with DFT methods, where only the lateral (i.e., stacked) dimers B and C were found to be energetically

(75) Fox, D. C.; Fiedler, A. T.; Halfen, H. L.; Brunold, T. C.; Halfen, J. A. *J. Am. Chem. Soc.* **2004**, *126*, 7627.
(76) Solomon, E. I.; Szilagyi, R. K.; George, S. D.; Basumallick, L. *Chem. Rev.* **2004**, *104*, 419.
(77) Fiedler, A. T.; Halfen, H. L.; Halfen, J. A.; Brunold, T. C. *J. Am. Chem. Soc.* **2005**, *127*, 1675.
(78) Brunold, T. C.; Solomon, E. I. *J. Am. Chem. Soc.* **1999**, *121*, 8277.
(79) Brunold, T. C.; Tamura, N.; Kitajima, N.; Moro-oka, Y.; Solomon, E. I. *J. Am. Chem. Soc.* **1998**, *120*, 5674.

Chart 3

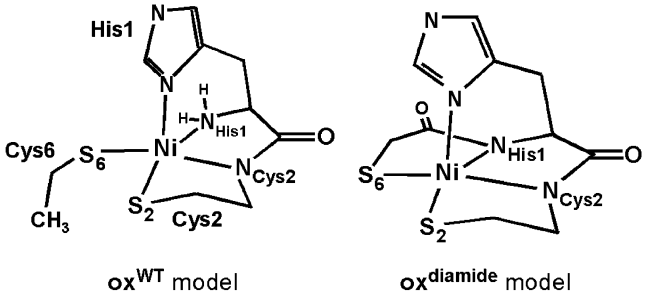

viable. Importantly, the DFT-computed frequencies for the breathing modes of the $[Ni^{3+}{}_2(\mu\text{-}S)_2]$ core of a truncated model of C are in good agreement with the experimental rR data (Figure 9). The tendency of these four-coordinate $[Ni^{3+}S_2N_2]$ complexes to form lateral dimers reflects a preference of Ni^{3+} centers for square-pyramidal coordination environments. This conclusion is further supported by the ability of added pyridine to coordinate strongly to the axial Ni^{3+} position of **2**, thereby yielding the monomer **2-py**.

Implications for the NiSOD Active Site. The insights gained from our studies of complexes **1**−**3** are also relevant to our understanding of the NiSOD active site because these models provide an excellent foundation for interpreting and evaluating spectroscopic data obtained for the enzyme. Specifically, given its success, the combined spectroscopic and computational approach that we have employed in this study to probe the electronic and spectral properties of the Ni^{3+} model complexes can now be applied to NiSOD. We have demonstrated above that DFT calculations provide reliable frequencies for the normal modes of nickel(3+) thiolate complexes and that the DFT-assisted vibrational peak assignments can be used to obtain metal−ligand force constants from NCAs of the experimental rR data. In this section, we apply this methodology to the vibrational data reported previously for oxidized NiSOD to obtain quantitative insights into the Ni−S/N bonding interactions at the enzyme active site.

The rR spectrum of as-isolated NiSOD exhibits three peaks at 349, 365, and 391 cm^{-1} associated with the ∼50% fraction of oxidized enzyme present in this form.[8] In our earlier study, we attributed the two lowest-energy peaks to the two Ni^{3+}−S stretching modes of the NiSOD active site because both are enhanced by excitation into the intense series of CT bands in the near-UV region of the absorption spectrum.[8] This assignment is confirmed here by our DFT calculations performed on our NiSOD model $\mathbf{ox^{WT}}$ (Chart 3), which yielded frequencies of 331 and 351 cm^{-1} for the two modes with predominately $Ni^{3+}-S_6$ and $Ni^{3+}-S_2$ stretching character, respectively (Table 4). Due to the fact that the mixed amine/amide ligation of the active site breaks the symmetry equivalence of the S and N ligands, the computed normal modes of NiSOD, unlike those of **1**−**3**, exhibit little coupling between the stretching motions of the cis bonds. Instead, the dominant Ni−S stretching motions in the 331 and 351 cm^{-1} modes are coupled, in a symmetric fashion, to the stretching motion of the trans Ni−N bonds (Table 4). The antisymmetric counterpart of the 331 cm^{-1} mode has a computed frequency of 389 cm^{-1}, and thus we assign the experimentally observed peak at 391 cm^{-1} to this normal mode. DFT also predicts a frequency of 414 cm^{-1} for the $Ni^{3+}-N_{amine}$ stretching mode (the antisymmetric counterpart to the 351 cm^{-1} mode). However, because the CT transitions of NiSOD contain virtually no contributions from $N_{amine} \rightarrow Ni^{3+}$ electronic excitations,[8] this mode is insufficiently resonance-enhanced to be discernible in the rR spectrum of NiSOD.

While the equatorial ligand sets of the NiSOD active site and the models **2** and **3** are quite similar, it is interesting that their respective rR spectra bear little resemblance to each other. For instance, the NiSOD spectrum exhibits no peaks below 300 cm^{-1} and its lowest-energy peak (at 349 cm^{-1}) has a higher frequency than nearly all of the peaks observed for **2** and **3**. In order to relate this trend to changes in force constants (i.e., bond strengths), we performed a NCA on a truncated model of the NiSOD active site, employing the normal-mode assignments given above. As shown in Table 5, the NCA-derived Ni−S stretching force constants of f_{Ni-S} = 1.68 and 1.79 mdyn $Å^{-1}$ are larger than those found for **2** and **3** by ∼10−20%, while the corresponding $Ni-N_{amide}$ force constant is larger by ∼5−10%. Thus, our quantitative analysis indicates that the $Ni-S/N_{amide}$ bonds at the $NiSOD_{ox}$

Table 4. Experimental and DFT-Calculated Frequencies and Normal-Mode Descriptions for Oxidized NiSOD ($\mathbf{ox^{WT}}$) and the Hypothetical Active-Site Model $\mathbf{ox^{diamide}}$

$NiSOD_{ox}$ ($\mathbf{ox^{WT}}$)				
exptl ν (cm^{-1})	calcd ν (cm^{-1})	Δ^a (cm^{-1})	Δ^b (%)	normal-mode description[c]
349	331	−18	−5	$Ni-S_6 + Ni-N_{Cys2}$
365	351	−14	−4	$Ni-S_2 + Ni-N_{His1}$
391	389	−2	−1	$Ni-N_{Cys2} - Ni-S_6$
N/A	413			$Ni-N_{His1} - Ni-S_2$

Hypothetical $NiSOD_{ox}$ model ($\mathbf{ox^{diamide}}$)	
calcd ν (cm^{-1})	normal-mode description
269	$Ni-S_2 - Ni-S_6$
328	$Ni-S_2 + Ni-S_6 + Ni-N_{Cys2} + Ni-N_{His1}$
400	$Ni-N_{Cys2} + Ni-N_{His1} - Ni-S_2 - Ni-S_6$
426	$Ni-N_{Cys2} - Ni-N_{His1}$

[a] Difference between DFT-calculated and experimental frequencies. [b] Same as footnote *a* but in relative units. [c] See Chart 3 for labeling scheme used.

Table 5. Summary of Metal−Ligand Stretching Force Constants

system	metal−ligand bond	force constant (mdyn $Å^{-1}$)[a]	ref
$NiSOD_{ox}$	$Ni^{3+}-S_2$	1.79	*b*
	$Ni^{3+}-S_6$	1.68	*b*
	$Ni^{3+}-N_{Cys2}$	1.34	*b*
2	$Ni^{3+}-S$	1.59	*b*
	$Ni^{3+}-N_{amide}$	1.21	*b*
3	$Ni^{3+}-S$	1.51	*b*
	$Ni^{3+}-N_{amide}$	1.28	*b*
blue copper[c]	$Cu^{2+}-S$	1.86	80
[Cu(S−^{t}Bu)(Tp)][d]	$Cu^{2+}-S$	1.90	81
rubredoxin	$Fe^{3+}-S$	1.24−1.36	82
ferredoxin	$Fe^{3+}-S_t$[e]	1.20−1.28	83

[a] 1 mdyn $Å^{-1}$ = 100 N/m. [b] This work. [c] Experimental data obtained from plastocyanin and azurin. [d] Tp = tris(3,5-diisopropyl-1-pyrazolyl)borate. [e] S_t refers to a terminal S_{Cys} donor.

active site are considerably stronger than those in the four-coordinate Ni^{3+} model complexes included in this study.

The origin of this difference probably lies in the unique coordination environment of the enzyme active site, since the replacement of an anionic deprotonated amide ligand by a neutral amine likely strengthens the remaining $Ni-S/N_{amide}$ bonds. To test this hypothesis, we generated a hypothetical computational model of the $NiSOD_{ox}$ active site (model $\mathbf{ox}^{\mathbf{diamine}}$) in which the amine ligand was converted to a deprotonated amide moiety (Chart 3). As expected, the DFT-computed frequencies and compositions of the normal modes for this model are remarkably similar to those found for **2** and **3** (Table 4). Significantly, the DFT-predicted frequencies for the $\mathbf{ox}^{\mathbf{diamine}}$ model are considerably lower than those computed for the original $\mathbf{ox}^{\mathbf{WT}}$ active-site model, indicating that the incorporation of a fourth anionic ligand does indeed weaken the remaining equatorial metal−ligand bonds to a significant degree.

Finally, when compared to other metalloproteins, it is apparent that the NiSOD active site contains among the strongest and most covalent metal−thiolate bonding interactions. In fact, the f_{Ni-S} stretching force constants of ∼1.7−1.8 mdyn $Å^{-1}$ determined for $NiSOD_{ox}$ rival the f_{Cu-S} values of ∼1.8−1.9 mdyn $Å^{-1}$ reported for blue copper active sites,[80,81] which are thought to possess the strongest metal−S_{Cys} bonds of any metalloenzyme active site. Moreover, the f_{Ni-S} values of $NiSOD_{ox}$ far exceed the f_{Fe-S} values typically found for iron(3+) thiolate units ($f_{Fe-S} \approx 1.25-1.35$ mdyn $Å^{-1}$; see Table 5).[82−84]

Acknowledgment. This research was supported by the NIH (Grant GM 64631), the Sloan Foundation Research Fellowship Program, and the NSF Graduate Research Fellowship Program. We thank Prof. Michael Maroney and Peter Bryngelson (University of Massachusetts−Amherst) for supplying us with the $[Ni(pdtc)_2][Et_4N]$ samples.

Supporting Information Available: Cartesian coordinates for all DFT geometry-optimized models (Tables S1−S9), polarized rR data for **1** (Figure S1), MCD spectra of "green" and "brown" samples of **2** (Figures S3 and S5, respectively), EPR spectra of **2-py** and **3** (Figure S4), TD-DFT-computed spectra for **1** and **2** (Figures S2 and S6), MO diagrams for **3** and [**3**$(MeCN)_2$] (Figure S7), and details concerning our NCAs for **1**−**3** and NiSOD. This material is available free of charge via the Internet at http://pubs.acs.org.

IC061237K

(80) Qiu, D.; Dasgupta, S.; Kozlowski, P. M.; Goddard, W. A.; Spiro, T. G. *J. Am. Chem. Soc.* **1998**, *120*, 12791.
(81) Qiu, D.; Kilpatrick, L. T.; Kitajima, N.; Spiro, T. G. *J. Am. Chem. Soc.* **1994**, *116*, 2585.
(82) Xiao, Y. M.; Wang, H. X.; George, S. J.; Smith, M. C.; Adams, M. W. W.; Jenney, F. E.; Sturhahn, W.; Alp, E. E.; Zhao, J. O.; Yoda, Y.; Dey, A.; Solomon, E. I.; Cramer, S. P. *J. Am. Chem. Soc.* **2005**, *127*, 14596.
(83) Han, S.; Czernuszewicz, R. S.; Kimura, T.; Adams, M. W. W.; Spiro, T. G. *J. Am. Chem. Soc.* **1989**, *111*, 3505.
(84) As described in ref 8, the unpaired electron in $NiSOD_{ox}$ resides in a $Ni^{3+}(z^2)$-based MO oriented along the $Ni-N_{ax}$ bond.